

2D Metal Oxyhalide-Derived Catalysts for Efficient CO₂ Electroreduction

F. Pelayo García de Arquer, Oleksandr S. Bushuyev, Phil De Luna, Cao-Thang Dinh, Ali Seifitokaldani, Makhsud I. Saidaminov, Chih-Shan Tan, Li Na Quan, Andrew Proppe, Md. Golam Kibria, Shana O. Kelley, David Sinton, and Edward H. Sargent*

Electrochemical reduction of CO₂ is a compelling route to store renewable electricity in the form of carbon-based fuels. Efficient electrochemical reduction of CO₂ requires catalysts that combine high activity, high selectivity, and low overpotential. Extensive surface reconstruction of metal catalysts under high productivity operating conditions (high current densities, reducing potentials, and variable pH) renders the realization of tailored catalysts that maximize the exposure of the most favorable facets, the number of active sites, and the oxidation state all the more challenging. Earth-abundant transition metals such as tin, bismuth, and lead have been proven stable and product-specific, but exhibit limited partial current densities. Here, a strategy that employs bismuth oxyhalides as a template from which 2D bismuth-based catalysts are derived is reported. The BiOBr-templated catalyst exhibits a preferential exposure of highly active Bi (1̄10) facets. Thereby, the CO₂ reduction reaction selectivity is increased to over 90% Faradaic efficiency and simultaneously stable current densities of up to 200 mA cm⁻² are achieved—more than a twofold increase in the production of the energy-storage liquid formic acid compared to previous best Bi catalysts.

Electrochemical reduction of CO₂ to fuels and feedstocks, powered using renewable sources of electricity, contributes to closing the carbon cycle.^[1–5] Specificity and productivity are measured via Faradaic efficiency (FE) and current density. Until now, the most productive electrocatalysts for formate—an attractive candidate as a liquid fuel and feedstock^[6–9]—are derived from noble metals such as palladium and silver.^[10–13]

Recent research efforts have focused on finding non-noble earth-abundant catalysts for formate production. Tin, bismuth,

and lead have shown high stability and selectivity.^[10,14–25] Despite the vast choice of catalysts, their productivity has generally not been sufficiently high.^[22] They have suboptimal binding energies for CO₂ reduction intermediates and suffer from by-product poisoning at certain facets. The extensive surface reconstruction of metal catalysts under high current operating conditions makes it particularly challenging to program specific favorable facets, active sites, and oxidation states, during operation.^[26–28]

Here, we report bismuth metal catalysts prepared via the in situ restructuring of 2D bismuth oxyhalides. The new catalysts exhibit enhanced specificity and productivity relative to previously reported bismuth catalysts.^[29] They reach current densities above 200 mA cm⁻² at over 90% FE in the electroproduction of formate.


We achieved this by taking advantage of 2D layered precursor materials—bismuth oxyhalides. The favorable formation energy of this precatalyst leads to selective reconstruction of in situ electroreduction to form high-surface-area petal-structured electrodes. This results in the preferential exposure of more active Bi (1̄10) facets, which we demonstrate with in situ grazing-incidence wide-angle X-ray scattering (GIWAXS) and X-ray absorption spectroscopy (XAS). This strategy increases the CO₂ reduction reaction specificity to over 90% while maintaining record-high current density (Table 1).

Dr. F. P. García de Arquer, Dr. O. S. Bushuyev, Dr. C.-T. Dinh, Dr. A. Seifitokaldani, Dr. M. I. Saidaminov, Dr. C.-S. Tan, Dr. L. N. Quan, A. Proppe, Dr. M. G. Kibria, Prof. E. H. Sargent
Department of Electrical and Computer Engineering
University of Toronto
35 St. George Street, Toronto, ON M5S 1A4, Canada
E-mail: ted.sargent@utoronto.ca

Dr. F. P. García de Arquer, Prof. D. Sinton
Department of Mechanical and Industrial Engineering
University of Toronto
5 King's College Road, Toronto, ON M5S 3G8, Canada

Dr. O. S. Bushuyev, Prof. S. O. Kelley
Leslie Dan Faculty of Pharmacy
Faculty of Medicine, Biochemistry
University of Toronto
Toronto, ON M5S 3M2, Canada

P. De Luna
Department of Materials Science Engineering
University of Toronto
27 King's College Circle, Toronto, ON M5S 1A1, Canada

 The ORCID identification number(s) for the author(s) of this article can be found under <https://doi.org/10.1002/adma.201802858>.

DOI: 10.1002/adma.201802858

Table 1. Performance comparison of various non-noble metals for CO₂ electroreduction to formate and best non-noble metal.

Catalyst	Current density [mA cm ⁻²]	Formate FE [%]	Citation
BiBrO templated	200	90+	This work
Metallic Bi	80	70	This work
Bi/ionic liquids	40	80	[19]
Bi/ionic liquids	12.5	90+	[36]
SnS derived	55	90+	[10]
SnO nanoparticles	200	64	[37]
Sn	200	90	[15]
CoO _x	10	90	[32]
Pb	62	95	[39]
Ag	300	60	[38]

In light of recent work reporting in situ formation of optimal CO₂RR catalysts via operando electro-redeposition,^[26,27] we explored bismuth-based compounds as a materials platform with which we could deliberately control the morphology to promote efficient catalysis. The bismuth oxide sheets making up oxyhalides (BiOX), where X = I, Br, Cl, are separated by negatively charged halogens (Figure 1a).^[30] We hypothesized

that these materials would, upon electroreduction, generate highly active ultrathin layers of metallic bismuth as the halogen layer is dynamically removed.^[29,31,32]

We prepared catalyst samples by coating the BiOBr in dimethyl sulfoxide (DMSO) solution onto carbon paper electrodes and annealing in an inert atmosphere (see Experimental Section). The crystal structure of the resulting pre-catalyst was confirmed using X-ray diffraction, and matched well with the calculated peaks for this structure (Figure 1b). The precursor catalysts were then electroreduced in CO₂-saturated aqueous KHCO₃ solutions via 10 cycles of cyclic voltammograms. After this electroreduction preconditioning, the sample consisted of a combination of Bi and minor Bi₂O₃ species, which was then used as a catalyst without further modification. X-ray photoemission spectroscopy (XPS) reveals the stoichiometry reconfiguration after sample hydration toward a Br-rich BiOBr, and the presence of residual Br in the reduced samples (Figure S1, Supporting Information). High-resolution transmission electron micrograph (HR-TEM) images reveal the presence of various BiOBr facets that selectively reconfigure into Bi (110) following conditioning (Figure 1c,d). Scanning electron micrograph (SEM) images of the BiOBr-templated catalysts before and after reconfiguration show a transition from an isotropic and amorphous configuration into a 2D ultrathin petal-like arrangement (Figure 1e,f).

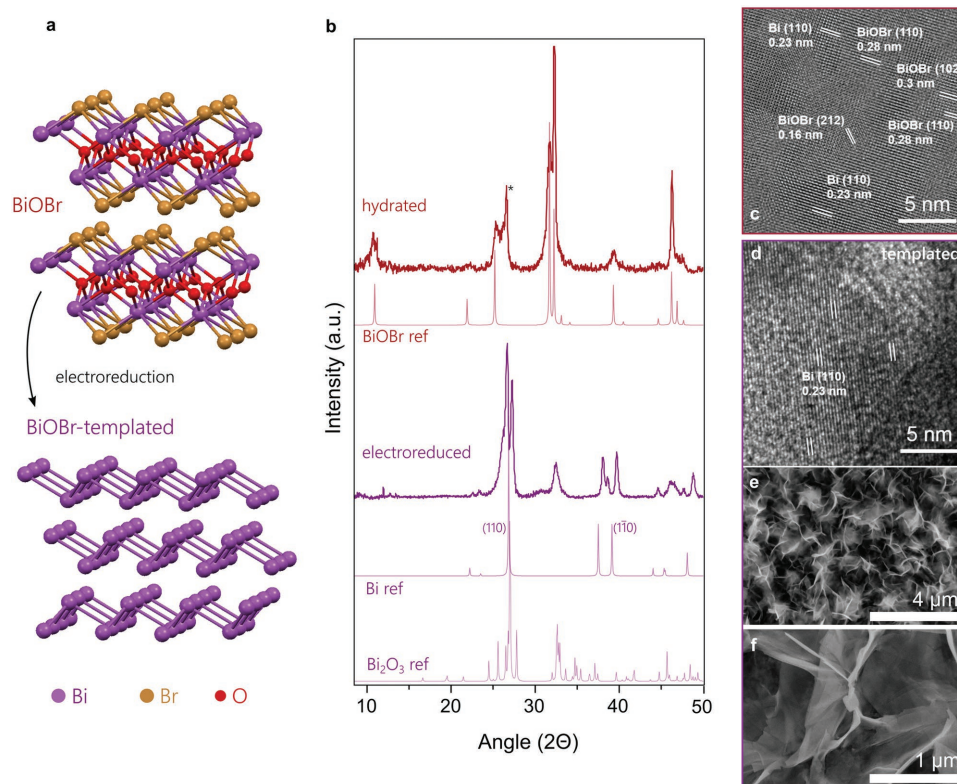


Figure 1. Bismuth oxyhalide-templated catalysts. a) Atomic structure of BiOBr and BiOBr-templated Bi catalyst after electroreduction. b) X-ray diffraction patterns of BiOBr pre-catalyst and BiOBr-templated samples, which are obtained after hydration of BiBr/carbon paper. The peak at 26° is that of the carbon support. BiOBr-templated catalysts are obtained by electroreducing BiOBr in a CO₂-purged electrolyte. The crystal structure of BiOBr-templated catalysts consists of a combination of Bi and Bi₂O₃ species. c, d) HRTEM before and after catalyst conditioning revealing the presence of different BiOBr facets (hydrated, before reaction) and their selective reconstruction into Bi after operation. e, f) SEMs of samples after reaction reveal a 2D petal-like layered arrangement after BiOBr electroreduction.

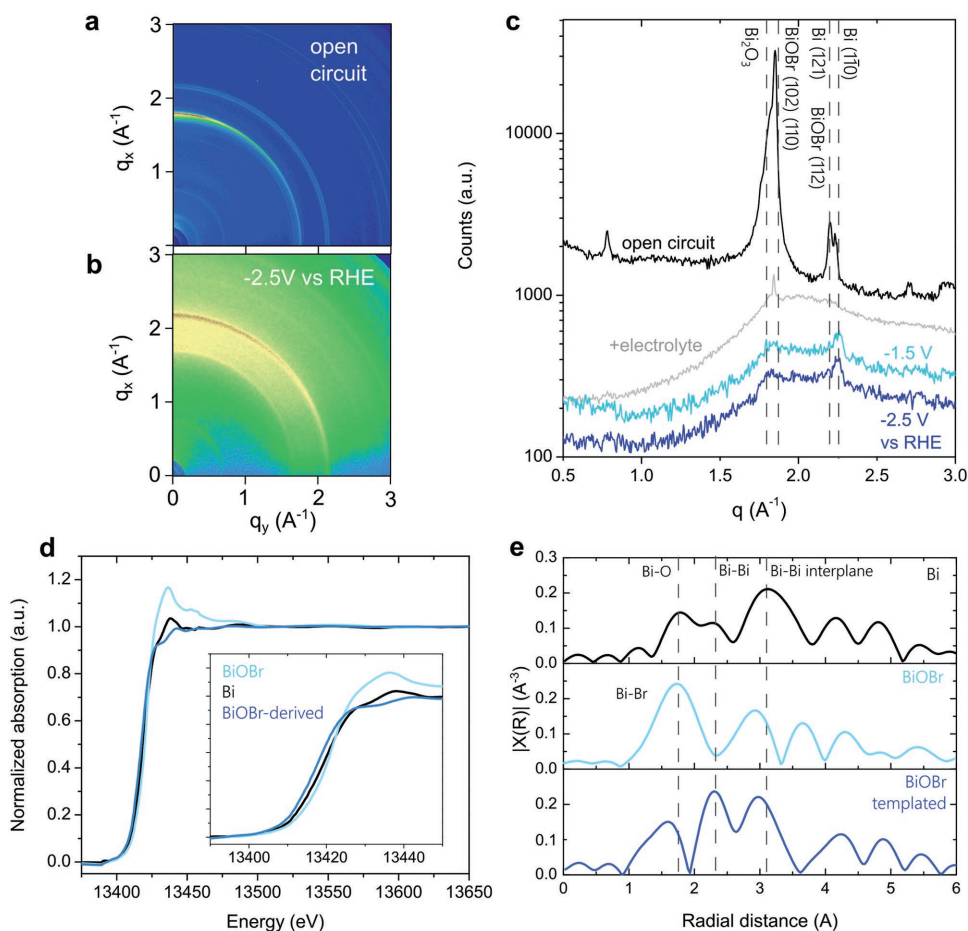


Figure 2. Surface reconstruction and in situ characterization of BiOBr-templated catalysts. a) In situ GIWAXS of BiOBr samples at open-circuit potential and b) under reducing potential versus RHE showcasing the catalyst reconfiguration. c) GIWAXS intensity along $q_y = 0$ revealing the drastic reduction of oxide and oxyhalide species and the dominant presence of Bi (110) and Bi (121) facets. This is supported by HRTEM measurements (Figure 1c,d). Near $q_y = 1.6 \text{ \AA}^{-1}$, various BiOBr and Bi-oxide contributions overlap. d) XANES of Bi L_3 transition revealing the different oxidation state of metal Bi and BiOBr-derived samples. e) EXAFS of Bi, BiOBr, and BiOBr-templated samples showing the increasing contribution of Bi–O bonds and compression of interplane Bi–Bi distances in BiOBr-derived samples.

To elucidate the structural evolution of the BiOX-templated catalyst at the atomic level, we carried out in operando GIWAXS measurements (Figure 2). BiOBr samples were placed in a custom-made reactor compatible with GIWAXS measurements and studied at different conditions (Figure 2a,b). At open-circuit conditions and in the absence of electrolyte, associated scattering peaks are seen in GIWAXS that we associate with BiOBr, Bi_2O_3 , and Bi species (Figure 2c). After we add 1 M KHCO_3 electrolyte, the signal-to-noise ratio decreases and only the peak associated with BiOBr remains.

We then operated the catalyst under increasingly reducing conditions. At -1.5 V versus reversible hydrogen electrode (RHE), there is a significant catalyst reconfiguration; Bi (110) facets become the dominant arrangement, with a suppression of bismuth oxide species and a decreased contribution of BiOBr. This is in agreement with the Pourbaix phase diagram of BiOBr at this operating condition (Figure S2, Supporting Information), which predicts a configuration consisting of Bi (s) and Br⁻ ions to be the most thermodynamically favorable.

To shed light on the electronic structure of the BiOBr-templated catalyst at operating conditions, we performed X-ray absorption near edge structure (XANES) and extended X-ray absorption fine structure (EXAFS) definition on BiOBr and Bi samples (Figure 2d). The absorption onset of the Bi L_3 transition shifts toward higher energy for BiOBr samples, which indicates an increasing oxidation state of as-prepared BiOBr compared to control Bi. BiOBr-templated samples exhibit a reduction in the oxidation state after operation consistent with BiOBr electroreduction. We resolved the Fourier transformed $|\chi(R)|$ spectrum to evaluate the density of neighboring atoms as a function of radial distance (Figure 2e).^[33] A different distribution of Bi–O, Bi–Br, and Bi–Bi bonds is evident for Bi, BiOBr, and BiOBr-templated samples. Both oxybromide and oxybromide-derived samples exhibit a modified presence of closer-distance oxide neighbors and an apparent Bi–Bi shortening. BiOBr samples possess their strongest peak at $R = 1.8 \text{ \AA}^{-1}$, which we attribute to the presence of O and Br neighbors. BiOBr-templated samples show a reduction in the density of these states, in agreement with XPS measurements,

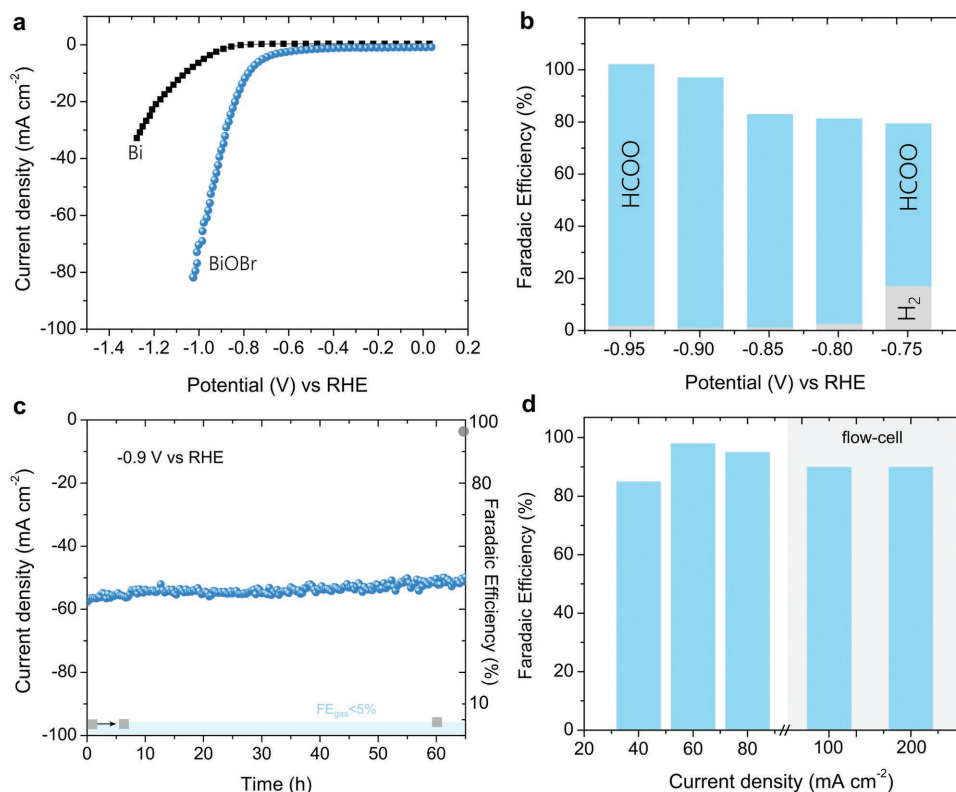


Figure 3. BiOBr-templated catalysts for efficient and stable CO₂ electroreduction. a) Linear-sweep voltammograms of BiOBr-templated catalysts versus thermally evaporated Bi control at 1 M KHCO₃ after iR correction. BiOBr samples exhibit a lower onset potential and a significantly higher current density. b) Product distribution for different operating potentials. H₂ production is suppressed after -0.75 V versus RHE, where only formate can be detected. At currents approaching 80 mA cm⁻², there is a rise in H₂ production due to CO₂ mass-transport limitations. Reference Bi samples, on the other hand, exhibit consistently a peak FE for formate lower than 75%. c) Current density trace at -0.9 V versus RHE potential. The FE for H₂ throughout the run is less than 4%, and the cumulative FE for formate approaches unity. d) FE as a function of current in H-cell and flow-cell configurations. An FE of 90% is sustained up to 200 mA cm⁻². The performance of other non-noble metal catalyst for CO₂ electroreduction is shown in Table 1 for comparison.

and instead exhibit two local maxima near 2.3 and 3.0 Å⁻¹. This is consistent with a Bi (110) configuration with an azimuthal compression, in contrast to bulk Bi control samples. We hypothesize that this favors the exposure of more active Bi facets as observed by in situ GIWAXS.

We then sought to evaluate the performance of the BiOBr-templated catalysts for CO₂ electroreduction. Testing of these catalysts in an aqueous H-cell set-up (0.1 M KHCO₃ electrolyte) revealed their higher activity compared to BiOX controls, exhibiting more than a twofold increase in current density, which led to 80 mA cm⁻² at -1.0 V versus RHE (Figure 3a). This approaches the CO₂ reduction current density limit achievable in the H-cell owing to CO₂ mass-transport limitations.^[34]

To study the activity of the catalyst with respect to operating potential, we analyzed the selectivity of BiOBr catalysts toward formate at different reducing potentials (Figure 3b). At potentials more negative than -1 V, hydrogen evolution accounted for less than 3% of product and CO production was totally suppressed. The maximum HCOO⁻:H₂ ratio was observed in the range of -0.8 to -1.0 V versus RHE after iR correction, with the formate FE reaching values over 99%. Liquid product analysis was performed using NMR in water suppression mode (see Experimental Section). Bi control samples, on the other hand, exhibited selectivities to formate of about 70% in this potential

range. BiOBr-templated catalysts exhibited remarkable stability, and retained their original performance during the course of an initial 65 h study at continuous operation (Figure 3c). This represents a twofold improvement in current density at near-unity FE compared to the best bismuth-based catalyst for CO₂ electroreduction into formate in traditional H-cell configurations. We also sought to switch the selectivity of BiOBr-templated catalysts toward CO and, when we operated it in an aqueous-free electrolyte, we achieved a similar productivity for this product (Figure S3, Supporting Information).

In view of the high current densities exhibited by BiOBr-templated catalyst, which reached CO₂ mass-transport limitations in an H-cell configuration, we developed catalysts that would work in a flow-cell system in which gas and liquid media are separated,^[4] overcoming mass transport in aqueous electrolytes and thus allowing a much higher CO₂RR current density and thus overall system productivity. To this end, we deposited BiOBr on top of a gas diffusion layer carbon electrode as a seed for the final BiOBr-templated catalyst. This allowed us to operate at much higher current densities in excess of 200 mA cm⁻² in a 2 M KHCO₃ electrolyte (Figure 3d and Figure S4, Supporting Information). The high selectivity toward formate remained largely unaffected, reaching a record value of 90% ± 5% even at these high current densities. Bi control

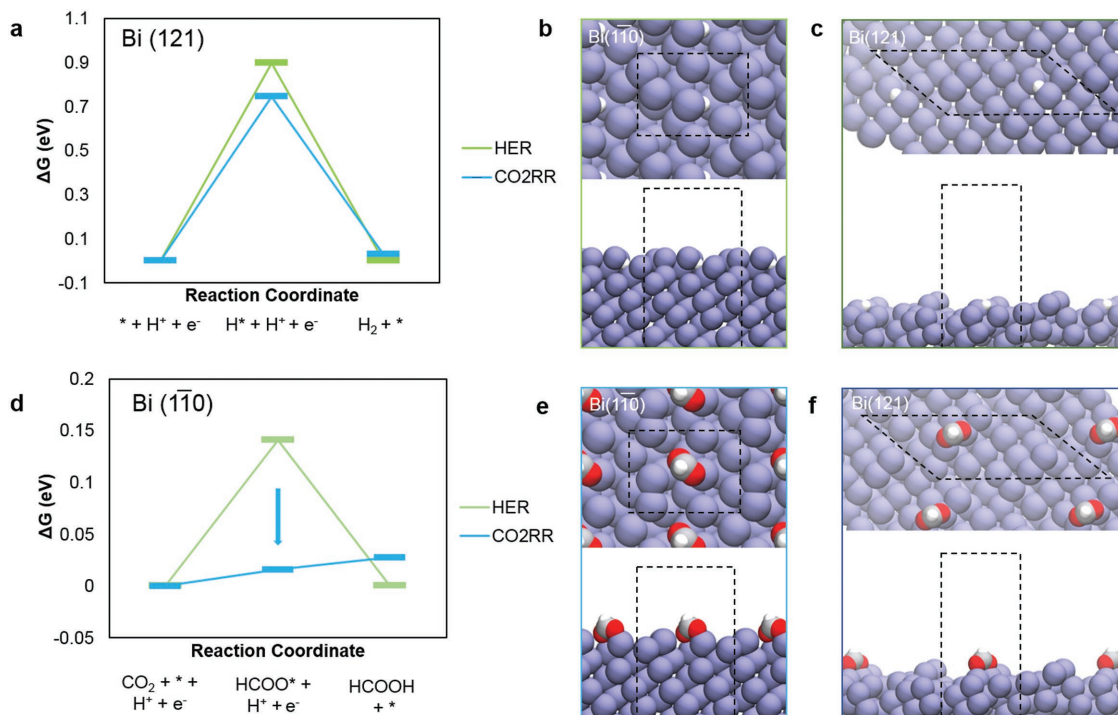


Figure 4. Reaction energy diagrams for HER (green) and CO₂RR to formic acid (blue) on a) Bi (121) and b) Bi ($\bar{1}\bar{1}0$) facets. Schematic of H* and HCOO* adsorption sites on d,e) Bi ($\bar{1}\bar{1}0$) and c,f) Bi (121). Bi ($\bar{1}\bar{1}0$) exhibits a preferential energy landscape for CO₂RR.

samples consistently exhibited lower current densities and formate selectivity around $70\% \pm 5\%$.

To provide further mechanistic insights into formate production on the BiOBr-templated catalyst, we performed density functional theory (DFT) calculations (Figure 4).^[35] Based on the operando GIWAXS experiments, we focused on the Bi (121) and Bi ($\bar{1}\bar{1}0$) facets to determine the effect of restructuring on the catalytic activity. From GIWAXS experiments, we found Bi (121) facet present in the precatalyst phase while Bi ($\bar{1}\bar{1}0$) emerged as the dominant facet during the operation. Only by measuring the surface facet structure under reaction conditions were we able to develop model metal slab models representative of the experimental catalyst. We sampled symmetric binding sites on the surface for both the HER (H*) and CO₂RR to formate (HCOO*) intermediates (Figures S5 and S6, Supporting Information) and chose the lowest energy structures for further analyses.

We explored the reaction energy pathways for CO₂ reduction to formate and the competing hydrogen evolution reaction (HER). Due to the near-unity experimental selectivity for formate, we did not focus on the CO production pathway. We found that the reaction energy barrier (ΔG) was significantly higher for both HER (0.90 eV) and CO₂RR (0.74 eV) on the Bi (121) facet. However, the Bi ($\bar{1}\bar{1}0$) facet displayed significantly lower reaction free energies for both HER (0.14 eV) and CO₂RR (0.03 eV). Importantly, the reaction energy barrier for CO₂RR to formate is the lowest of all reactions on the Bi ($\bar{1}\bar{1}0$) facet with the rate determining step being the second proton-coupled electron transfer to the bound HCOO* intermediate. Additionally, the stepped Bi ($\bar{1}\bar{1}0$) surface offers near-optimal Gibbs free binding energies for HCOO* (-0.01 eV) close to the thermodynamic minimum. The GIWAXS, electrocatalytic experiments, and DFT

studies taken together point toward the promotion of a highly active surface facet during CO₂ reduction that favors formic acid production to the exclusion of competing products.

In conclusion, we demonstrate a new catalyst design strategy beginning with bismuth oxyhalides as a template from which we derived 2D bismuth-based materials, enabling the realization of catalysts that can sustain simultaneously high selectivity and activity for CO₂ electroreduction. We employed in situ GIWAXS measurements to demonstrate that BiOBr-templated catalysts exhibit a preferential exposure of more highly active Bi ($\bar{1}\bar{1}0$) facets. We thereby achieve a high selectivity toward formate over 90% that remains up to current densities as high as 200 mA cm^{-2} , demonstrating the potential of metal oxyhalide-templated catalysts for the efficient electroreduction of CO₂.

Experimental Section

An extensive description of materials, sample fabrication and characterization, product analysis and computational studies, can be found in Supporting Information.

Supporting Information

Supporting Information is available from the Wiley Online Library or from the author.

Acknowledgements

F.P.G.d.A., O.S.B., and P.D.L. contributed equally to this work. This work was supported by the Canadian Institute for Advanced Research (CIFAR) Bio-inspired Energy Program, the Ontario Research Fund

(ORF-RE-08-034), and the Natural Sciences and Engineering Research Council (NSERC) of Canada. The authors thank the Canadian Light Source (CLS) for support in the form of a travel grant. Computations were performed on the SOSCIP Blue Gene/Q computing platform. SOSCIP is funded by the Federal Economic Development Agency of Southern Ontario, the Province of Ontario, IBM Canada Ltd., Ontario Centres of Excellence, Mitacs, and 15 Ontario academic member institutions. The authors thank X. Gong, J. Li, R. Quintero-Bermudez, P. Cheng, J. Li, L. Levina, R. Wolowiec, D. Kopilovic, and E. Palmiano for their help over the course of this research. M.I.S. acknowledges the support of Banting Postdoctoral Fellowship Program, administered by the Government of Canada. O.S.B. and P.D.L. acknowledge the financial support in the form of the NSERC Postdoctoral Fellowship and Canada Graduate Scholarship–Doctoral (CGS D) Award, respectively. Research described in this paper was performed at the Canadian Light Source, which is supported by the Canada Foundation for Innovation, Natural Sciences and Engineering Research Council of Canada, the University of Saskatchewan, the Government of Saskatchewan, Western Economic Diversification Canada, the National Research Council Canada, and the Canadian Institutes of Health Research. Connaught Fund of the University of Toronto.

Conflict of Interest

The authors declare no conflict of interest.

Keywords

2D materials, catalysis, CO₂ electroreduction, formate, metal oxyhalides

Received: May 3, 2018

Revised: July 12, 2018

Published online:

- [1] S. I. Seneviratne, M. G. Donat, A. J. Pitman, R. Knutti, R. L. Wilby, *Nature* **2016**, 529, 477.
- [2] S. Chu, Y. Cui, N. Liu, *Nat. Mater.* **2017**, 16, 16.
- [3] O. S. Bushuyev, P. De Luna, C. T. Dinh, L. Tao, G. Saur, J. van de Lagemaat, S. O. Kelley, E. H. Sargent, *Joule* **2018**, 2, 825.
- [4] D. M. Weekes, D. A. Salvatore, A. Reyes, A. Huang, C. P. Berlinguette, *Acc. Chem. Res.* **2018**, 51, 910.
- [5] Z. W. Seh, J. Kibsgaard, C. F. Dickens, I. Chorkendorff, J. K. Nørskov, T. F. Jaramillo, *Science* **2017**, 355, eaad4998.
- [6] M. Jouny, W. Luc, F. Jiao, *Ind. Eng. Chem. Res.* **2018**, 57, 2165.
- [7] S. Verma, B. Kim, H.-R. “Molly” Jhong, S. Ma, P. J. A. Kenis, *ChemSusChem* **2016**, 9, 1972.
- [8] J. Eppinger, K.-W. Huang, *ACS Energy Lett.* **2017**, 2, 188.
- [9] J. T. Feaster, C. Shi, E. R. Cave, T. Hatsukade, D. N. Abram, K. P. Kuhl, C. Hahn, J. K. Nørskov, T. F. Jaramillo, *ACS Catal.* **2017**, 7, 4822.
- [10] X. Zheng, P. De Luna, F. P. García de Arquer, B. Zhang, N. Becknell, M. B. Ross, Y. Li, M. N. Banis, Y. Li, M. Liu, O. Voznyy, C. T. Dinh, T. Zhuang, P. Stadler, Y. Cui, X. Du, P. Yang, E. H. Sargent, *Joule* **2017**, 1, 794.
- [11] A. Klinkova, P. De Luna, C.-T. Dinh, O. Voznyy, E. M. Larin, E. Kumacheva, E. H. Sargent, *ACS Catal.* **2016**, 6, 8115.
- [12] R. Kortlever, I. Peters, S. Koper, M. T. M. Koper, *ACS Catal.* **2015**, 5, 3916.
- [13] X. Liu, J. Xiao, H. Peng, X. Hong, K. Chan, J. K. Nørskov, *Nat. Commun.* **2017**, 8, 15438.
- [14] Y. Zhang, L. Chen, F. Li, C. D. Easton, J. Li, A. M. Bond, J. Zhang, *ACS Catal.* **2017**, 7, 4846.
- [15] D. Kopljár, A. Inan, P. Vindayer, N. Wagner, E. Klemm, *J. Appl. Electrochem.* **2014**, 44, 1107.
- [16] S. Y. Choi, S. K. Jeong, H. J. Kim, I.-H. Baek, K. T. Park, *ACS Sustainable Chem. Eng.* **2016**, 4, 1311.
- [17] Y. Zhang, F. Li, X. Zhang, T. Williams, C. D. Easton, A. M. Bond, J. Zhang, *J. Mater. Chem. A* **2018**, 6, 4714.
- [18] J. L. DiMaggio, J. Rosenthal, *J. Am. Chem. Soc.* **2013**, 135, 8798.
- [19] A. Atifi, D. W. Boyce, J. L. DiMaggio, J. Rosenthal, *ACS Catal.* **2018**, 8, 2857.
- [20] J. Shang, W. Hao, X. Lv, T. Wang, X. Wang, Y. Du, S. Dou, T. Xie, D. Wang, J. Wang, *ACS Catal.* **2014**, 4, 954.
- [21] N. Hollingsworth, S. F. R. Taylor, M. T. Galante, J. Jacquemin, C. Longo, K. B. Holt, N. H. de Leeuw, C. Hardacre, *Angew. Chem., Int. Ed.* **2015**, 54, 14164.
- [22] A. J. Martín, G. O. Larrazábal, J. Pérez-Ramírez, *Green Chem.* **2015**, 17, 5114.
- [23] E. Irtem, T. Andreu, A. Parra, M. D. Hernández-Alonso, S. García-Rodríguez, J. M. Riesco-García, G. Penelas-Pérez, J. R. Morante, *J. Mater. Chem. A* **2016**, 4, 13582.
- [24] M. Fan, S. Garbarino, G. A. Botton, A. C. Tavares, D. Guay, *J. Mater. Chem. A* **2017**, 5, 20747.
- [25] E. Bertin, S. Garbarino, C. Roy, S. Kazemi, D. Guay, *J. CO₂ Util.* **2017**, 19, 276.
- [26] P. De Luna, R. Quintero-Bermudez, C.-T. Dinh, M. B. Ross, O. S. Bushuyev, P. Todorovi, T. Regier, S. O. Kelley, P. Yang, E. H. Sargent, *Nat. Catal.* **2018**, 1, 103.
- [27] P. Grosse, D. Gao, F. Scholten, I. Sinev, H. Mistry, B. Roldán Cuenya, *Angew. Chem.* **2018**, 130, 6300.
- [28] D. Ren, J. Fong, B. S. Yeo, *Nat. Commun.* **2018**, 9, 925.
- [29] W. Bi, C. Wu, Y. Xie, *ACS Energy Lett.* **2018**, 3, 624.
- [30] X. Meng, Z. Zhang, *Mater. Lett.* **2018**, 225, 152.
- [31] J. Li, Y. Yu, L. Zhang, *Nanoscale* **2014**, 6, 8473.
- [32] S. Gao, Y. Lin, X. Jiao, Y. Sun, Q. Luo, W. Zhang, D. Li, J. Yang, Y. Xie, *Nature* **2016**, 529, 68.
- [33] P. Rabe, *Jpn. J. Appl. Phys.* **1978**, 17, 22.
- [34] T. Burdyny, P. J. Graham, Y. Pang, C.-T. Dinh, M. Liu, E. H. Sargent, D. Sinton, *ACS Sustainable Chem. Eng.* **2017**, 5, 4031.
- [35] J. S. Yoo, R. Christensen, T. Vegge, J. K. Nørskov, F. Studt, *ChemSusChem* **2016**, 9, 358.
- [36] C. W. Lee, J. S. Hong, K. D. Yang, K. Jin, J. H. Lee, H.-Y. Ahn, H. Seo, N.-E. Sung, K. T. Nam, *ACS Catal.* **2018**, 8, 931.
- [37] C. Liang, B. Kim, S. Yang, Y. L. Yang Liu, C. Francisco Woellner, Z. Li, R. Vajtai, W. Yang, J. Wu, P. J. A. Kenis, P. M. Ajayan, *J. Mater. Chem. A* **2018**, 6, 10313.
- [38] A. Seifitokaldani, C. M. Gabardo, T. Burdyny, C.-T. Dinh, J. P. Edwards, M. G. Kibria, O. S. Bushuyev, S. O. Kelley, D. Sinton, E. H. Sargent, *J. Am. Chem. Soc.* **2018**, 140, 3833.
- [39] X. Lu, D. Y. C. Leung, H. Wang, M. M. Maroto-Valer, J. Xuan, *Ren. Energy* **2016**, 95, 277.